Slot die coating of polybenzimiazole based membranes at the air engulfment limit
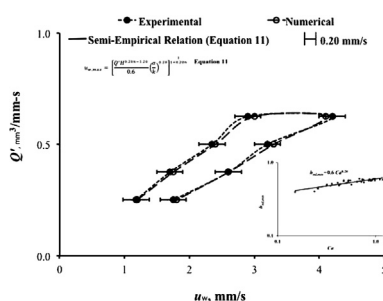
Kanthi Latha Bhamidipati, Sima Didari, Tequila A.L. Harris*

George W. Woodruff School of Mechanical Engineering, Georgia Institute of Technology, Atlanta, GA 30332, USA

HIGHLIGHTS

- Air engulfment in shear-thinning solutions is investigated.
- A semi-empirical model is derived to predict air engulfment velocity.
- Smaller coating gap or higher operating temperature enable larger coating speed.
- Air engulfment can be delayed by employing solutions with higher surface tension.

GRAPHICAL ABSTRACT

ABSTRACT

The objective of the current study is to analyze the slot die coating process of highly viscous (1–20 Pa s), shear-thinning solutions. The upper and lower coating boundaries are determined with respect to various non-dimensional parameters. Polyphosphoric acid doped polybenzamidazole (PPA/PBI) solutions are used as the test solutions. Simulations are performed using 2D, volume-of-fluid (VOF) model available in FLUENT 6.3.26 to predict the coating windows. The numerically predicted coating window compared within ±4% of the experimental data. Design of Experiments (DOE) is performed to understand the impact of operational and processing conditions on the coating windows. It is observed that the air engulfment could be delayed by using smaller coating gaps and higher processing temperatures, which would facilitate faster processing of thin films, an important attribute during industrial scale processing. One major contribution from the study is the development of a semi-empirical model, in which operational and processing parameters are supplied as inputs to predict the air engulfment velocity within ±10% accuracy.

© 2013 Elsevier B.V. All rights reserved.

1. Introduction

Slot die coating classified as a pre-metered coating technique, is successfully being used for manufacturing a broad range of thin films such as photographic films, papers [1], coatings on glass substrates [2], optical films for liquid crystal displays (LCD) [3], fuel cell membranes [4–6], etc. As shown in Fig. 1, in this method, a solution with a predetermined flow rate, (Q_{in}) is suspended from a slot die onto a substrate moving at speed (u_w). The coated film attains a constant thickness downstream of the die, which is called the wet thickness (h). One of the main advantages of slot die coating is that the coating thickness is pre-metered and controlled, meaning the final coating thickness is determined from the flow rate through the slot die and the substrate speed [7,8].

A limited range of operating conditions, for which high quality films are produced, exists for slot die coating as defined by the "coating window" as shown in Fig. 2. Outside the coating window, various types of defects such as dripping, air entrainment, and break lines will be formed [9–11]. Dripping corresponds to the top most boundary of the coating window and occurs when the flow

* Corresponding author. Tel.: +1 404 385 6335; fax: +1 404 894 9342.
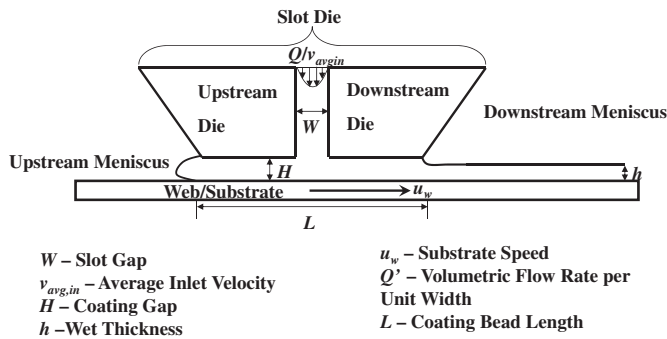E-mail address: tequila.harris@me.gatech.edu (T.A.L. Harris).

W – Slot Gap
$v_{avg,in}$ – Average Inlet Velocity
H – Coating Gap
h –Wet Thickness

u_w – Substrate Speed
Q' – Volumetric Flow Rate per
Unit Width
L – Coating Bead Length

Fig. 1. Schematic of the slot die coating process from the point of fully developed flow between parallel plates [6].

rate is too high relative to the substrate speed causing the solution to collect behind the upstream die, and creep up the outer wall of the upstream die. When dripping occurs, the pre-metering characteristic of the slot die is lost since the thickness of the film can no longer be controlled. Because of the limitation posed by air entrainment on the coating speed, which is an important factor in improving the production rates of the thin film, it is considered as a major defect encountered during slot die coating, especially for high-viscosity solutions (i.e., solution having a capillary number, (Ca, >0.1) [11]. At higher substrate speeds, air bubbles get entrained between the substrate and the liquid film [12,13]. In some cases, the air bubble is restricted to only a fraction of the total film thickness, while in other cases; the bubble extends all the way to the top of the film resulting in a hole [6]. Extending the coating speed beyond the air entrainment value results in the formation of break lines [14,15]. It has been found that as the coating speed increases, the originally straight contact line breaks into "vee" structures (also termed as sawteeth), and the air bubbles eventually break up from the tip of these sawteeth [6,12,16]. Some researchers [17,18] employed vacuum at the upstream end to delay air entrainment, however, air entrainment in this study corresponds to the no-vacuum conditions as is the case with other studies [10,15,19,20].

At a given flow rate, the range of the wet thickness of defect-free films is restricted by the air entrainment/break lines and dripping. Maximum wet thickness (h_{max}) is achievable at the minimum substrate speed ($u_{w,min}$), and the minimum wet thickness (h_{min}) is obtained at the highest coating speed ($u_{w,max}$). Lee et al. [21] found that in the slot die coating of the Newtonian solutions, the dimensionless minimum wet thickness ($h_{nd,min} = h_{min}/H$), increases as capillary number ($Ca = \mu u_{w,max}/\sigma$) increases until a critical capillary number, Ca^*, is reached (Region I). Beyond Ca^*, the dimensionless minimum wet thickness was found to be only a function of coating gap and was independent of capillary number (Region II). Carvalho and Kheshgi [17] found that by increasing the

capillary and Reynolds numbers beyond the values reported by Lee et al. [21], there was another region in which the dimensionless minimum wet thickness decreases with capillary number (Region III). Experiments performed by Chang et al. [15] show that the transition from Region I to Region II will occur around $Re = 1$, and the transition from Region II to Region III will occur around $Re = 20$. Furthermore, while moderate and high-viscosity fluids followed Regions I and II, low viscosity solutions followed Regions II and III [15]. Region I was primarily dominated by viscous and surface tension forces [22] and the transition from Region I to Region II had competing viscous and inertial forces. Region II was influenced predominantly by inertial forces. The inertial forces grew significantly from Region II to Region III, such that the fluid exiting the slot die resembled a jet impinging on a moving substrate.

Gutoff and Kendrick [9] studied the effect of the non-Newtonian behavior of coating solutions on the coating window using polyvinylalcohol (PVA) solutions. They found that compared to the coating windows obtained using Newtonian solutions, the width of the coating window increased for non-Newtonian solutions. In the study, it was shown that the maximum coating speed increased by about an order for the non-Newtonian solution. Ning et al. [10] found that for an optimum polymer concentration in glycerin-water solutions, the maximum coating speeds can be achieved. On the other hand, experiments and simulations performed by Romero et al. [23] on high molecular weight polymers in dilute solutions showed that as the extensional viscosity of the coated liquid increases, the width of the coating window decreases. Existing literature regarding the effect of the surface tension on the coating window is inconclusive, due to the contradicting findings by various researchers. Gutoff and Kendrick [9] reported that surface tension does not play a significant role on the coating window and it only impacts the shape of the coating bead. According to Hamers et al. [24], solutions with lower surface tension assisted in widening the coating window, while studies performed by Tiu et al. [25] and Chu et al. [26] found the opposite trend; i.e., solutions with higher surface tension form more stable coating beads, extending the coating window.

To understand the effects of operational parameters like slot gap (W) and coating gap (H) on the size of the coating window, Lee et al. [21] conducted various experiments with the silicon oil solution. They found that a smaller coating gap and higher coating speeds will increase the coating windows and that the slot gap had negligible effect. Chang et al. [19] showed that for solutions with viscosities of 0.075 Pa s and 0.2 Pa s, smaller minimum wet thickness values were attainable if smaller coating gaps were used. However, they found that the effect of coating gap was insignificant for solution with viscosities lower than 0.003 Pa s.

Several theoretical and numerical studies have been conducted to understand the coating process. Ruschak [27] performed the first theoretical study to predict coating windows for pre-metered coating processes. Higgins and Scriven [28] extended the study to include viscous effects. Both studies assume the flow field to be steady and completely two-dimensional.

Saito & Scriven [29] and Carvalho & Kheshgi [17] used two-dimensional, finite element methods to analyze slot die coating of Newtonian solutions. Similar models were employed by Romero et al. [8,18,23,30] to predict the coating windows for Newtonian fluids, mildly viscoelastic fluids, and high molecular weight polymer fluids. In some of these studies [18,23,30], the slot die parallel-plate regions and the upstream regions are excluded from the computational domain, following the findings by Carvalho and Kheshgi that these regions (slot die parallel-plate regions and the upstream regions) have no impact on the operating conditions at low capillary and Reynolds numbers. These assumptions pertaining to the computational domain prevent extracting data on the
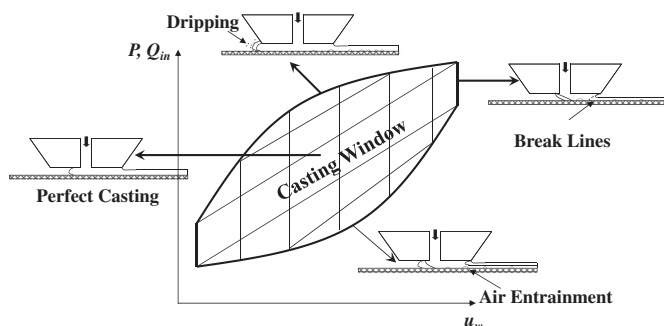

Fig. 2. Illustration of the coating window [6].

upstream meniscus and the dynamic contact line, which is important in understanding the type of defects. In addition, the studies assume that the downstream meniscus is pinned to the die lip, while in reality the downstream meniscus is free to move [14,15,19,20]. Chang et al. [15] also showed that the location of the downstream meniscus is important in determining the three minimum wet thickness regions.

Chu et al. [14] and Chang et al. [22] used Flow-3D software to perform 2D simulations for predicting the air entrainment speed and the time taken for the upstream and downstream menisci to reach their final steady state positions respectively. The limitation of this model is that while the meniscus shape is solved by applying force balance, the actual air entrainment mechanism was not captured.

More generic and simplified models like the 1D, lubrication model and the model available in TopCoat software could not predict air entrainment velocity accurately. The major limitation of these and the previously mentioned models is that they do not solve the multiphase equations necessary to capture air entrainment, which is crucial in accurately determining the air entrainment velocity. The air entrainment velocity in such studies corresponded to either an upstream contact angle of nearly 180° [14] or a downstream contact angle of nearly 10° [18,23]. Another limitation of the models is that they assume steady state conditions, while air entrainment is inherently unsteady.

The volume-of-fluid (VOF) method was developed by Hirt and Nichols [31] to overcome the shortcomings of former methods such as height functions, line segments and marker particles. Hirt and Richardson [32], Harris & Bhamidipati [33] and Bhamidipati & Harris [34–36] used a transient, volume-of-fluid (VOF) model to effectively predict the air entrainment velocity. Bhamidipati [37] used both 2D and 3D transient, VOF simulations employing FLUENT 6.3.26, and concluded that the overall coating window predictions including air entrainment velocity hardly varied between the two.

The maximum dynamic viscosity of the solutions used to study the coating processes by earlier researchers has been limited to around 1 Pa s [9,10,19,23]. Since many polymer-based solutions used in the coating processes have much higher viscosities, the current study focuses on the coating behavior of shear-thinning, non-Newtonian solutions with viscosities ranging between 1 Pa s and 20 Pa s, to understand if reported trends hold for such solutions. The effects of the operational and processing parameters on the coating process of such high viscous solutions are investigated numerically and experimentally.

The slot die coating process is simulated using a 2D transient VOF model available in FLUENT 6.3.26. The numerical results are validated experimentally using in-built, customized experimental setup. The effects of the slot die operational properties such as slot gap and coating gap, the material properties such as the degree of non-Newtonian behavior and surface tension of the solutions on the coating window are studied. A semi-empirical model is derived, to predict the upper coating window limit, described by the onset of air entrainment. At the threshold of air entrainment, the coating bead will break which results in the formation of an unsteady contact line and the engulfment of air bubbles inside the coated film. In the current study this type of entrainment is investigated and predicted by the numerical simulation. The predictions obtained from the numerical model are finally validated using one set of experiments.

2. Material properties

Polyphosphoric acid doped polybenzamidazole (PPA/PBI) solutions, which are used in high temperature polymer electrolyte membrane fuel cells, are used to coat the substrate during the slot die coating process, which are later hydrolyzed to form phosphoric acid doped polybenzamidazole membranes. PPA/PBI solutions are extremely viscous at room temperature having a viscosity as high as 4500 Pa s, and hence are typically processed above 120 °C, to significantly decrease the viscosity during processing [38]. The material and physical properties were measured at 120 °C, 140 °C and 160 °C. The material properties of the PPA/PBI solutions were evaluated at Augustine Scientific Laboratory in Newbury, Ohio, under controlled relative humidity of 55%. The viscosity of PPA/PBI was measured using a Brookfield LV Viscometer with a small volume UL Accessory, for shear rates between 2 s^{-1} and 120 s^{-1}. As shown in Fig. 3, it is evident that the solutions have non-Newtonian shear-thinning behavior, which can be defined by the power-law model given as:

$$\eta_{app} = k\dot{\gamma}^{n-1} \tag{1}$$

where k is the consistency index and n is the power-law index.

The density and surface tension of PPA/PBI were measured using the quartz rod displacement method on a Kruss Processor Tensiometer K100 and Wilhelmy plate on a Kruss Processor Tensiometer K100 method, respectively. The slot die is made of 316 stainless steel and the moving substrate is polyterephthalate (PET). The contact angles with respect to 316 stainless steel and PET were measured by using the sessile drop method on a Kruss Drop Shape Analysis System (DSA) 100. The results are reported in Table 1.

3. Experimental set-up and procedure

3.1. Experimental setup

A custom designed and built roll feed imaging system (RFIS) [39], was used experimentally to analyze the coating process on the PPA/PBI thin films. The RFIS generally consists of the following subsystems: (a) roll-feed and web control subsystem to control the speed and tension of the webbing, (b) tooling subsystem to produce the extrusion with a temperature- and pressure-controlled tank, die, and piping, (c) temperature control subsystem to ensure tank, die, and platen temperatures during coating, and (d) inspection subsystem to monitor the quality of the manufactured product. More details can be found in Ref. [39].

3.2. Experimental procedure

The coating solution is heated in a vacuum oven to the desired temperature. Simultaneously, the tooling subsystem and the
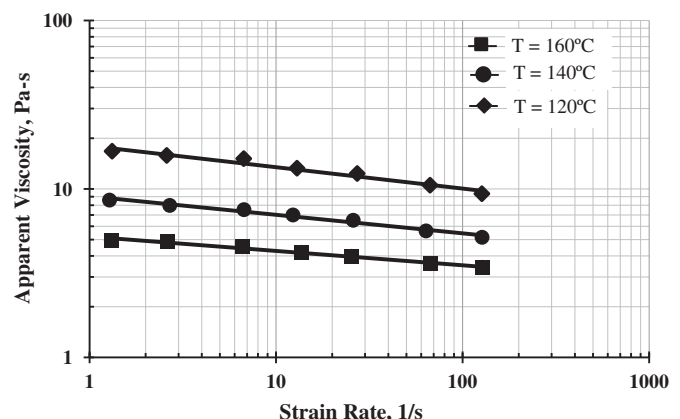
Fig. 3. Apparent viscosity of PPA/PBI at $T = 120$ °C, 140 °C and 160 °C.

Table 1
Properties of polybenzimidazole doped polyphosphoric acid solution.

Properties	PPA/PBI at 120 °C	PPA/PBI at 140 °C	PPA/PBI at 160 °C
ρ (kg m^{-3})	1952.7	1947.5	1942.1
σ (N m^{-1})	0.0475	0.0467	0.0461
θ_s °	33.2	31.6	30.5
θ_{sd} °	92.3	91.5	90.9

substrate are heated to the same temperature. After adjusting the slot gap and the coating gap, and pouring the solution into the pressure vessel, the vessel is pressurized to a desired value using a nitrogen tank, while a ball valve is at off position. To coat the film, the ball valve is opened and the solution is allowed to flow at a preset flow rate through the slot die until it contacts the moving substrate. To obtain the coating window, the substrate speed at which dripping occurs is recorded first, and then it is slowly increased while keeping the pressure value constant, until air bubbles are noticed, so the minimum and maximum substrate speeds are determined by the onset of dripping and air entrainment, respectively. The process is repeated to obtain the two boundary points at different pressure values. Due to the fluctuation of the pressure reading for the pressure below 3 psi, all the tests were performed at pressure above 3 psi. The maximum substrate speed is restricted to 15 mm s^{-1} to avoid external noise factors resulting from the structural vibration and instability of the system at higher substrate speeds. The volumetric flow rate of the coating solution through the slot die corresponding to the applied pressure is obtained by measuring the weight of the solution coated on the PET substrate in a given time interval, then subtracting the weight of the uncoated PET and dividing the resultant by the density of the coating solution. In order to nullify the impact of the die width, all results are presented in terms of the volumetric flow rate divided by the die width, Q'.

4. Modeling approach

The slot die coating process involves displacement of air by the coating solution resulting in a two-phase flow field. The two-phase flow field is simulated using the VOF model available in FLUENT 6.3.26 [40] for tracking interfaces between the fluids. In the VOF model, the volume fraction scalar α, the volume occupied by a fluid in a given domain to the total volume of the domain, of the given fluid is solved in every computational cell. The volume fraction equals one when the cell is completely filled with the fluid and equals zero when the cell is devoid of the fluid. As both fluids are present at the interface, the volume fraction varies between zero and one at the interface. The model solves for the volume fraction, α_{cs}, of the PPA/PBI solution using Equation (2) given as:

$$\frac{\partial \alpha_{cs}}{\partial t} + \boldsymbol{u} \cdot \nabla \alpha_{cs} = 0 \tag{2}$$

where the subscript 'cs' stands for coating solution, t is time and $\boldsymbol{u}$ is the velocity vector. Since the volume fractions for the two phases equals one in a two-phase flow field, the air volume fraction, α_{air}, is given by:

$$\alpha_{air} = 1 - \alpha_{cs} \tag{3}$$

After the volume fractions are computed, the interface is reconstructed using the geometric reconstruction (Geo-Reconstruct) method developed by Young [41]. The Geo-Reconstruct method, which uses a piecewise-linear interface construction (PLIC) scheme is the most accurate model available in FLUENT 6.3.26 [40] to construct interfaces [41], and obtain discrete air

pockets [34]. Geo-Reconstruction scheme requires that Equation (2) to be discretized explicitly in time and the advection terms of Equation (2) to be rewritten in terms of fluxes through the faces, then the slope of the interface between the two fluids, coating solution and air, in any given cell (calling the given cell, cell$_{i,j}$) is computed using the volume fractions from the surrounding cells and the volume fraction of the cell itself. The volume fractions at the four faces of cell$_{i,j}$ are computed using a linear interpolation between cell$_{i,j}$ and each of the other four cells which share a face with cell$_{i,j}$. Once the volume fractions are obtained on the bounding faces, the slope of the interface in cell$_{i,j}$ is then calculated using the four faces volume fractions, as slope $= \alpha_{f,r} - \alpha_{f,l}/\alpha_{f,u} - \alpha_{f,d}$ where $\alpha_{f,r}$, $\alpha_{f,l}$, $\alpha_{f,u}$, and $\alpha_{f,d}$ are the volume fractions of the faces at the right, left, top and bottom sides of the cell, respectively. The interface is then adjusted such that the ratio of volume occupied by air to the volume occupied by coating solution is equal to the volume fraction of the air.

The velocity vector field is solved using the continuity and momentum equations as given by Equations (4) and (5) respectively:

$$\frac{\partial \rho}{\partial t} + \nabla \cdot (\rho \boldsymbol{u}) = 0 \tag{4}$$

$$\frac{\partial (\rho \boldsymbol{u})}{\partial t} + \nabla \cdot (\rho \boldsymbol{u} \boldsymbol{u}) = -\nabla P + \nabla \cdot \mathfrak{T} + \rho \boldsymbol{g} + \boldsymbol{F_s} \tag{5}$$

where ρ is the density, $\mathfrak{T}$ is the stress tensor, P is the pressure, $\boldsymbol{g}$ is acceleration due to gravity and $\boldsymbol{F_s}$ is a momentum source term used to capture the surface tension effects. The continuum surface force model (CSF) developed by Brackbill [42] is used to account for the surface tension, σ, in the source term $\boldsymbol{F_s}$ and treat it as a three-dimensional effect across the interface. Based on the CSF model, the source term, $\boldsymbol{F_s}$, is given by:

$$\boldsymbol{F_s} = \sigma \frac{\kappa \nabla \alpha_{cs}(\alpha_{cs}\rho_{cs} + \alpha_{air}\rho_{air})}{0.5(\rho_{air} + \rho_{cs})} \tag{6}$$

where the curvature, κ is given by the divergence of the unit normal at the interface, $\widehat{\boldsymbol{n}}_{if}$ as given by Equation (7):

$$\kappa = \nabla \cdot \widehat{\boldsymbol{n}}_{if} = \nabla \cdot (\boldsymbol{n_{nl}}\cos\theta + \boldsymbol{n_t}\sin\theta) \tag{7}$$

where $\boldsymbol{n_{nl}}$ is normal to the wall, $\boldsymbol{n_t}$ is tangent to the wall and θ is the contact angle between the coating solution and wall, when measured inside the coating solution.

Viscosity and Density (indicated by φ) that appear in the continuity and momentum equations are averaged using Equation (8):

$$\varphi = \alpha_{cs}\varphi_{cs} + \alpha_{air}\varphi_{air} \tag{8}$$

Viscosity of the coating solution is captured using the power-law fluid available in FLUENT 6.3.26, the details of which are presented by Bhamidipati et al. [6].

Velocity at the interface, $\boldsymbol{u}$ is computed using Equation (9):

$$\boldsymbol{u} = \frac{\alpha_{air}\rho_{air}\boldsymbol{u}_{air} + \alpha_{cs}\rho_{cs}\boldsymbol{u}_{cs}}{\alpha_{air}\rho_{air} + \alpha_{cs}\rho_{cs}} \tag{9}$$

To simulate the experimental conditions, the temperature is maintained constant throughout the computational domain; hence, energy equation is not solved.

4.1. Computational domain

As illustrated in Fig. 4, the computational domain used in the current study primarily consists of the downstream section of the
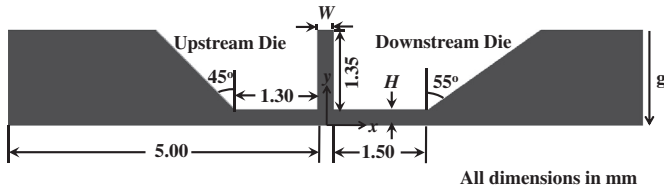
Fig. 4. Illustration and dimensions of the computational domain.

slot die, the substrate and the region between the slot die and the substrate. The domain is extended in the downstream direction to ensure fully developed conditions exist. The upstream boundary is extended by the same extent to guarantee the same pressure drop across the upstream and downstream regions. The dimensions of the computational domain are also shown in Fig. 4, since, the slot gap, W and coating gap, H are variables whose effects on air engulfment velocity are studied, they are listed as variables on Fig. 4. As explained previously, the study is performed using a 2D domain. This assumption is considered to be valid, since, the width (normal to the page) of the slot die used in the experiments is about two-orders higher than the slot gap and coating gap.

4.2. Boundary conditions

The locations where the relevant boundary conditions are applied are illustrated in Fig. 5.

(1) A fully developed velocity profile, $v(x)$, developed for a power-law fluid is defined at the inlet:

$$v(x) = \frac{(2n+1)}{(n+1)} \left\{ 1 - \left(\frac{2x}{W}\right)^{(n+1)/n} \right\} \frac{Q'}{W}$$

where Q' is the volumetric flow rate per unit width of the slot die, n is the power-law index, W is the slot gap and x is the distance measured from the origin as shown in Fig. 5.

(2) Atmospheric pressure conditions (gauge pressure of zero) are simulated at the upstream end, downstream end and top surfaces (excluding the angled slot die walls) to simulate atmospheric conditions:

$$P_g = 0.$$

(3) At the liquid/gas interface, the sum of the capillary pressure and hydrostatic pressure on the air side, P_{air} balances the normal stress in the coating solution, $\mathscr{T}_{cs}$

$$\mathscr{T}_{cs} = \frac{1}{Ca}\hat{n}\nabla\cdot\hat{n} - \hat{n}P_{air}$$

$$Ca = \frac{k\left(\frac{u_w}{H}\right)^{(n-1)} u_w}{\sigma}$$

Since there cannot be any mass transfer across the interface:

$$\hat{\mathbf{n}}\cdot\mathbf{u} = 0$$

(4) The no-slip boundary condition is specified everywhere on the slot die and the PET walls except at the static and dynamic contact lines.

$$\mathbf{u} = \mathbf{u_w}$$

(5) As shown by several researchers [43–45], stress singularity is an issue at the contact lines. However, as the stress is integrable at the static contact line [46], no-slip boundary condition can be applied at the static contact line [47], which is the condition specified in this study. In addition, the static contact angle boundary condition is set.

(6) The stress singularity is however not integrable at the dynamic contact line [47]. This limitation has been overcome in previous work [48–56] by applying a slip condition at the dynamic contact line. However, for a shear-thinning fluid like the ones used in the current study, Rosenblat & Davis [54] and Weidner & Schwartz [57] showed that the singularity is integrable. Nevertheless, a slip condition has to be applied at the dynamic contact line since there is a relative velocity of the contact line with respect to the substrate during the coating process. Hence, the boundary condition at the PET wall (including the dynamic contact line) is specified using the slip formulation of Kistler [47]:

$$u = f(x)u_c + [1 - f(x)]u_w$$

where $f(x)$ is a function of space variable "x", and given by:

$$f(0) = 1 \text{ and}$$

$$f(x) = 0 \quad \text{for } x \geq \Delta x,$$

where Δx is the slip length. The interval size of the mesh at the contact line, in the x-direction is set as the slip length. u_c is the contact line velocity and u_w is the substrate velocity. The contact angle at the dynamic contact angle boundary is set equal to the angle made by the coating solution with the PET substrate.

The transient 2D VOF simulation is conducted assuming a variable time step and a courant number of 1. SIMPLE scheme is selected for the pressure–velocity coupling, and pressure and velocity are discretized using PRESTO and second order upwind methods, respectively. The under-relaxation factors of 0.2, 1, 1 and 0.5 are selected for pressure, density, body force and momentum terms. To accurately predict the maximum coating speeds a fine mesh is required. The mesh size used for the conducted numerical simulations in this study is selected based on stability, time efficiency and accuracy of the numerical predictions compared to the experimental data, as reported in Ref. [6].

To obtain the coating window, numerically, the substrate speed is changed, while the inlet flow rate is kept constant. Then substrate speed which corresponds to the dripping boundary is determined
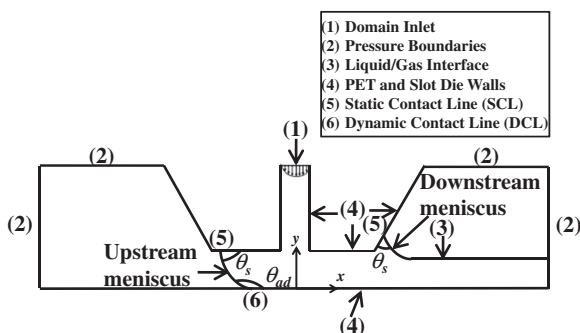

Fig. 5. Locations where boundary conditions are specified.

Table 2
Parameters used in DOE study for the PPA/PBI solutions.

Name	Units	Level 1	Level 2	Level 3
W	mm	0.178	0.25	0.30
H	mm	0.178	0.25	0.30
T	°C	120	140	160

by tracking the location of the upstream meniscus, when solution flows beyond the upstream die lip the corresponding substrate speed is set as the boundary. The maximum coating speed is determined when air is engulfed inside the coated film, typically shown in the upstream meniscus as an air pocket between the interface of the substrate and the solution.

5. Results and discussion

A design of experiments (DOE) approach was used to perform the simulations in order to understand the impact of slot gap (W), coating gap (H) and processing temperature (T) on the air engulf-ment velocity of PPA/PBI solution during slot die coating. Specifically, a fractional factorial DOE based on Taguchi's design is performed. For each of the three parameters, three values are used as listed in Table 2. Taguchi's fractional factorial design generated nine runs using various combinations of W, H and T as listed in Table 3.

5.1. Dimensional coating windows

The coating windows generated for the nine DOE runs with respect to processing temperatures, 120 °C, 140 °C and 160 °C, are presented in Fig. 6(a)–(c) respectively. For any given slot gap and coating gap combination, the ratio of the flow rate per unit width, Q', to the dripping velocity, $u_{w,min}$, is found to be a constant on the dripping boundary, which made the dripping boundary on the coating window a line with a constant slope. The maximum coating speed was obtained when Run 5 conditions were used, due to the higher processing temperature, which results in a lower viscosity of the solution. This is consistent with earlier findings [7,9,21]. The effect of W and H on the air engulfment velocity is however not evident from the coating windows. In order to understand the impact of the operational parameters, the data is presented in a non-dimensional form as discussed in Section 5.2.

One objective of the coating process is to get a wide range of thicknesses for a given set of operational conditions and processing temperature in order to have greater processing versatility. From the DOE runs, the maximum (h_{max}) and minimum (h_{min}) wet thicknesses were obtained by dividing the flow rate per unit width, Q' by the corresponding substrate speeds, u_w. $u_{w,min}$ is used for obtaining h_{max} corresponding to dripping boundary and $u_{w,max}$ is used for obtaining h_{min} corresponding to air engulfment boundary. h_{max} is independent of Q', since the slope of the dripping boundary is a constant. It is found that h_{min} decreases as Q' decreases. Therefore, for a given set of conditions and parameters, smaller flow rates produce wider range of thicknesses. Both the minimum and maximum wet thicknesses were found to increase with an increasing coating gap, which has to be expected, since the solution has to fill the coating gap region before it reaches the final

Table 3
Runs generated for DOE.

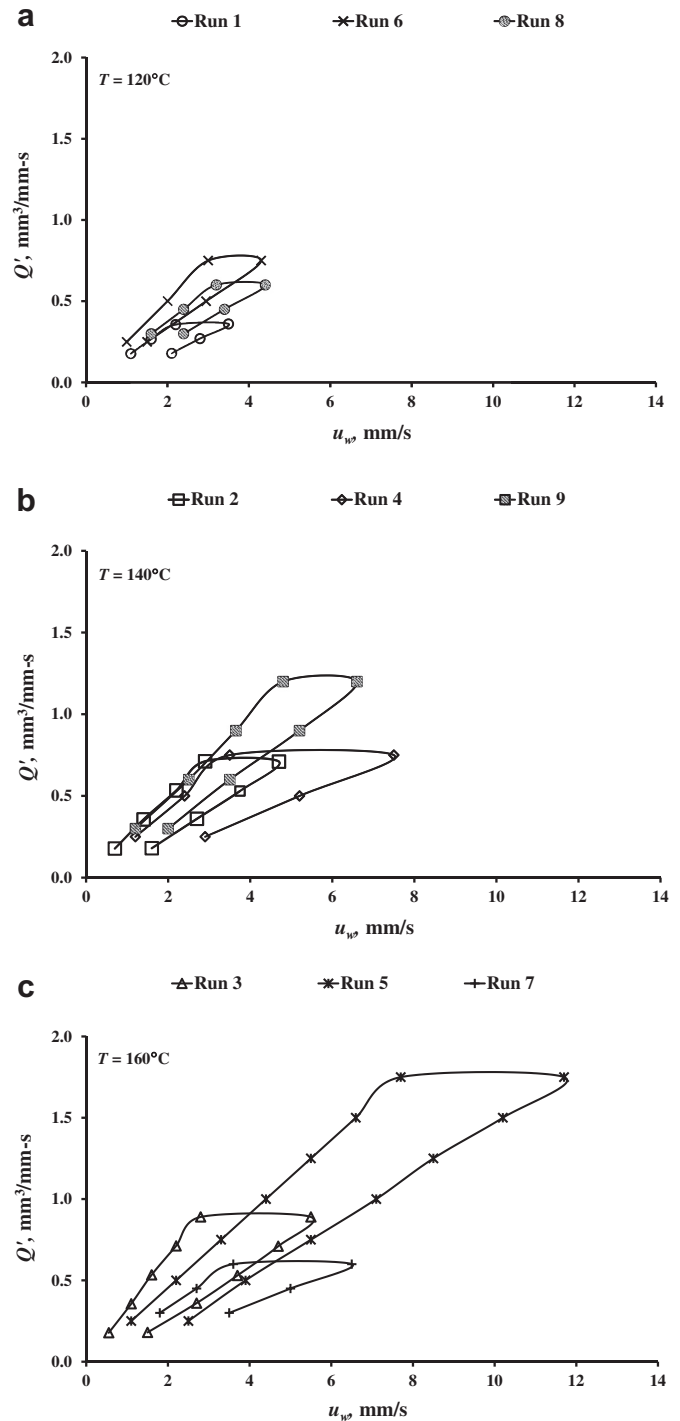| Run #	1	2	3	4	5	6	7	8	9
W, mm	0.178	0.178	0.178	0.25	0.25	0.25	0.3	0.3	0.3
H, mm	0.178	0.25	0.3	0.178	0.25	0.3	0.178	0.25	0.3
T, °C	120	140	160	140	160	120	160	120	140

Fig. 6. (a) Coating windows obtained for the DOE runs at 120 °C, 1, 6 and 8. (b) Coating windows obtained for the DOE runs at 140 °C, 2, 4 and 9. (c) Coating windows obtained for the DOE runs at 160 °C, 3, 5 and 7.

thickness. Run 3, of the DOE, produced the widest range of thick-nesses due the lower viscosity and larger coating gap, compara-tively. For Run 3, h_{max} was 0.33 and h_{min} was 0.12, thus the difference was 0.21, which is 25–75% wider than the other runs.

5.2. Non-dimensionalized coating window

The effects of the operational parameters (W and H) on the air engulfment velocity were analyzed by plotting the non-
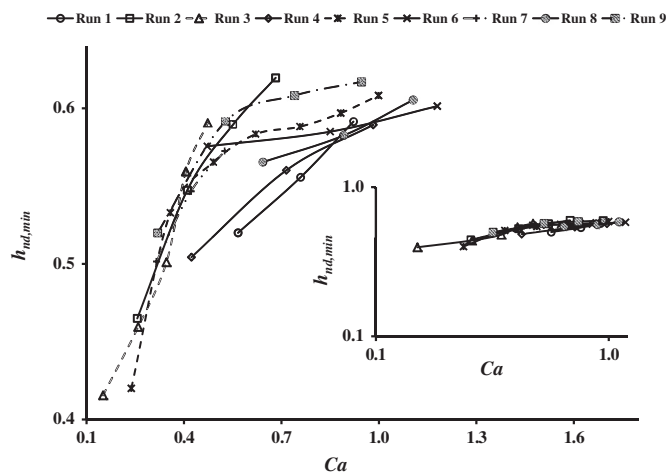
Fig. 7. Dimensionless minimum wet thickness versus capillary number on a logarithmic scale.

Fig. 8. Power-law curve-fitting between minimum wet thickness and capillary number.

dimensionalized minimum wet thickness as a function of the capillary number, as shown in Fig. 7. The non-dimensionalized minimum wet thickness is obtained by dividing the minimum wet thickness with the coating gap. The dimensionless minimum wet thickness was found to increase with increasing capillary number. Earlier findings [15] also showed that high-viscosity solutions follow Region I, where the minimum wet thickness increases with capillary number. Given the insignificant differences between the non-dimensionalized plots, it can be deduced that true non-dimensionality exists between the dimensionless minimum wet thickness and the capillary number. Comparing the dimensional coating windows (Fig. 6(a)–(c)) to the dimensionless coating window (Fig. 7), it can be further deduced that the end of the coating window on the air engulfment side is reached either when the dimensionless minimum wet thickness reaches a value between 0.55 and 0.60 or the capillary number approaches 1.2. The restriction on the dimensionless minimum wet thickness arises from the fact that during slot die coating, the downstream die lip acts as a doctor blade, which inhibits thickening of the coated film beyond a certain limit [21]. Hence, the slot die is also referred to as the metered-knife coater [58]. The limitation on the capillary number is due to an imbalance between the viscous and the capillary forces. While the viscous forces cause the coating solution to be pulled in the direction of substrate motion, capillary forces arising from the surface tension property of the solution drag the solution in the other direction. Therefore, as the viscous forces dominate over the capillary forces such that the capillary number exceeds 1.2, instability of the upstream meniscus occurs resulting in air engulfment. The limitation on the capillary number was also noticed by Wilkinson [59].

A power-law equation is obtained between the dimensionless minimum wet thickness and the capillary number by fitting a curve through the data points presented in Fig. 7. As depicted in Fig. 8 the resulting equation is given as:

$$h_{\mathrm{nd,min}} = 0.6 \, Ca^{0.20} \tag{10}$$

This semi-empirical relation corresponds to the minimum wet thickness that can be attained by a film before defects appear. Since the semi-empirical relation was derived by fitting a curve through all the data points obtained from the DOE study, the curve-fit does not go through all the data points and compares within ±10% of the actual data from the DOE study.
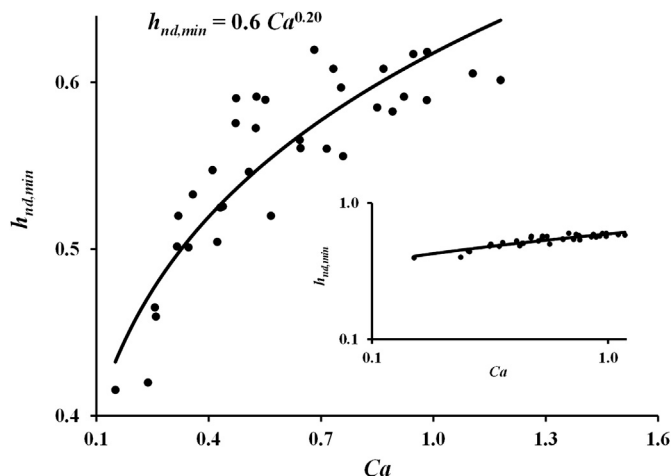
The accuracy of the semi-empirical model is tested by comparing the model predictions with experimental data reported by Chang et al. [15], numerical data reported by Lin et al. [20], and the visco-capillary model reported by Higgins and Scriven [28]. The operational parameters and the coating solution properties used in the relevant studies are listed in Table 4.

The plots from the validation study are presented in Fig. 9. The semi-empirical model predicted the results of Chang et al. [15] and Lin et al. [20] within ±15%. The relatively higher differences between the semi-empirical model and the studies from the literature [15,20] could be due to a difference in the rheology of the solutions. In addition, the solutions used in the current study follow Region I, while the solutions from literature are in the transition zone between Regions I and II. The comparison between the predictions from the semi-empirical model and the visco-capillary model shows that even though the trends match qualitatively, the semi-empirical model over-predicts the data. However, the higher values predicted by the semi-empirical model can be justified because vacuum is applied behind the upstream die in the study by Higgins and Scriven [28], while no vacuum is applied in the current study. When vacuum is applied, the air engulfment is postponed to higher values, resulting in smaller minimum thicknesses.

From the aforementioned findings, the semi-empirical model given by Equation (10) can be used for predicting the minimum wet thickness of the coated solution within certain constraints. (a) The minimum dimensionless thickness should not exceed a value between 0.55 and 0.6. For example, when the semi-empirical model predictions are compared with the data by Chang et al. [19] and Lee et al. [21], whose minimum wet thickness values exceed 0.6, the semi-empirical model under-predicts the results. (b) The data obtained in the current study is limited to a capillary number range of 0.15–1.2. The validity of the model below a capillary number of 0.15 needs to be investigated, which is not done in the current study. (c) The dimensionless minimum wet thickness should either follow Region I or is in the transition between Region I and Region II. According to the findings by Chang et al. [15], the location of the downstream meniscus determines the region followed by the

Table 4
Details of the studies used for validation of semi-empirical model.

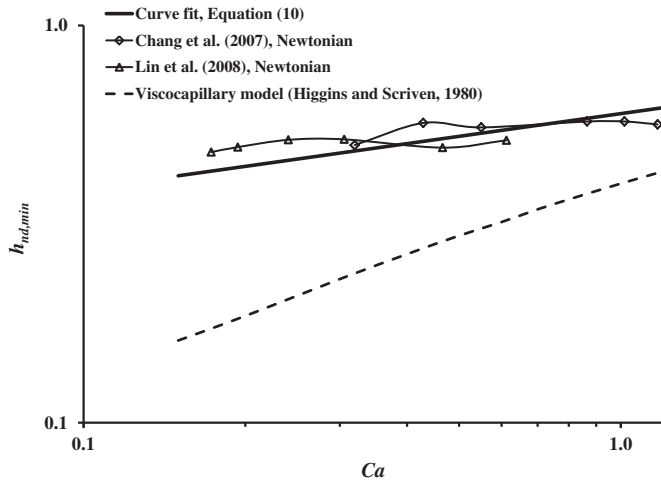| Data Source	Nature of Solution	W, mm	H, mm
Chang et al. [13]	Newtonian ($\mu = 0.05$ Pa s, $\sigma = 0.067$ N m^{-1})	0.20	0.20
Lin et al. [18]	Newtonian ($\mu = 0.20$ Pa s, $\sigma = 0.0665$ N m^{-1})	0.20	0.20

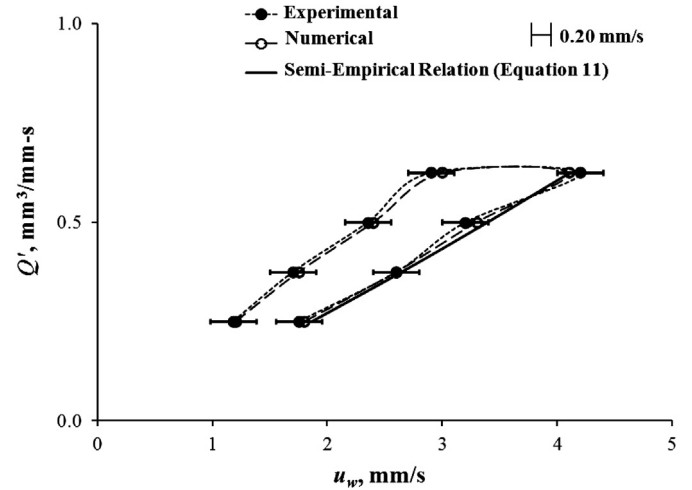**Fig. 9.** Validation of the semi-empirical relation, Equation (10), with experiments and literature.

Fig. 10. Comparison of coating windows obtained experimentally and numerically at $W = 0.25$ mm, $H = 0.25$ mm and $T = 120$ °C. The solid line represents the maximum coating speed obtained from Equation (11).

minimum wet thickness. Chang et al. [15] showed that for a solution that falls under Region I, the downstream meniscus creeps up the downstream die. Similar observations were made in this study.

5.3. Validation of numerical and semi-empirical models with experiment

The semi-empirical model is rearranged into a dimensional form to obtain an explicit equation in terms of maximum coating speed (air engulfment velocity) as given by Equation (11), which can be easily compared to the experimental results.

$$u_{\text{W,max}} = \left[\frac{Q'H^{0.20n-1.20}}{0.6} \left(\frac{\sigma}{k} \right)^{0.20} \right]^{\frac{1}{1+0.20n}} \tag{11}$$

Using the experimental procedure outlined in Section 3.2, an experiment was conducted. The PPA/PBI solution was coated on to the moving substrate at 120 °C for $W = 0.25$ mm and $H = 0.25$ mm. Simulations were performed to obtain a complete coating window at the same conditions. The coating window obtained experimentally is compared with the coating window obtained through simulations, as shown in Fig. 10. In addition, the maximum coating speeds obtained from the semi-empirical relation given by Equation (11) is compared. The numerical model predicted the experimental coating window within ±4%, while the semi-empirical model predicted the maximum coating speed within ±5% of the experimental values. The uncertainty in measuring the flow rate per unit width, Q', during the experiments is found to be very trivial at 0.0025 m^3 mm^{-1} s^{-1}. The main uncertainty in the experimental values is in the measurement of the coating speed as represented by the error bars in Fig. 10.

5.4. Effect of operational and processing parameters on the air engulfment velocity

In the following subsections, the effects of slot gap (W), coating gap (H), consistency index (k), power-law index (n) and surface tension (σ) on air engulfment velocity are presented.

5.4.1. Effect of slot gap

The effect of slot gap on the maximum coating speed is not directly evident from Equation (11), as it indirectly enters the equation through Q' where $Q' = W \times v_{\text{in}}$. However, for a given flow

rate per unit width, Q', as the slot width, W reduces, average inlet velocity, v_{in} adjusts itself such that their product is constant. This implies that the slot width does not impact the maximum coating speed for a given Q'. Fig. 11 shows the effect of slot width on the maximum coating speed for $H = 0.30$ mm and the three slot gaps, $W = 0.178$ mm, 0.25 mm, and 0.30 mm using PPA/PBI solution at 160 °C, which confirms this hypothesis. The discrete points represent the data from the simulations, while the solid black line is based on Equation (11). Maximum coating speed ceases to exist for relatively smaller slot gaps at higher flow rates, as the end of coating window is reached due to the occurrence of dripping, due to the higher velocity. Since, the slot gap has no impact on the maximum coating speed, it can be implied that the inertia forces have negligible impact on the maximum coating speed, which is consistent with the findings by Lee et al. [21].

5.4.2. Effect of coating gap

According to Equation (11), the maximum coating speed, $u_{\text{W,max}}$, varies inversely with the coating gap, H. This effect can be
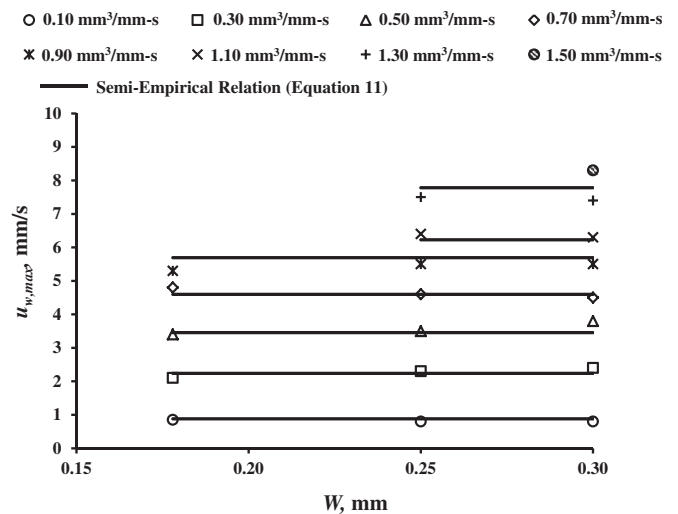

Fig. 11. Effect of slot gap, W, on the maximum coating speed, $u_{\text{W,max}}$ for various flow rates per unit width, Q' at $H = 0.30$ mm and $T = 160$ °C. The discrete data points represent the simulation results, while the solid lines are obtained from Equation (11).

○ 0.18 mm³/mm-s   □ 0.27 mm³/mm-s   △ 0.36 mm³/mm-s   ◇ 0.45 mm³/mm-s
✳ 0.54 mm³/mm-s   ✕ 0.63 mm³/mm-s   + 0.72 mm³/mm-s   ◎ 0.81 mm³/mm-s
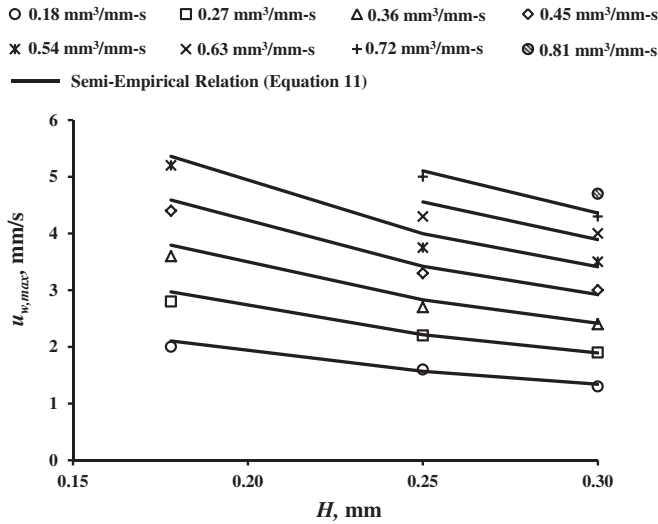—— Semi-Empirical Relation (Equation 11)

Fig. 12. Effect of coating gap, H, on the maximum coating speed, $u_{w,max}$ for various flow rates per unit width, Q' at $W = 0.178$ mm and $T = 140\ °C$. The discrete data points represent the simulation results, while the solid lines are obtained from Equation (11).

confirmed from Fig. 12, which show the plots at $W = 0.178$ mm, $T = 140\ °C$ and Q' ranging from 0.18 mm³ mm⁻¹ s⁻¹ to 0.81 mm³ mm⁻¹ s⁻¹. Similar observations were made by Lee et al. [21] and Chang et al. [15,19]. Primarily, there are two advantages associated with coating a power-law fluid at smaller coating gaps. (1) Surface tension driven capillary forces are stronger for smaller coating gaps, thus stabilizing the contact line and delaying the air engulfment; and (2) As the power-law fluid moves through a smaller coating gap, the viscosity of the solution drops owing to the power-law nature of the fluid, resulting in higher maximum coating speed.

On the other hand, delayed dripping that occurs at larger coating gaps due to the ability to accommodate more fluid can facilitate processing at higher flow rates. Also, as noted in Section 5.1, larger coating gaps can be used to obtain a wide range of thicknesses.
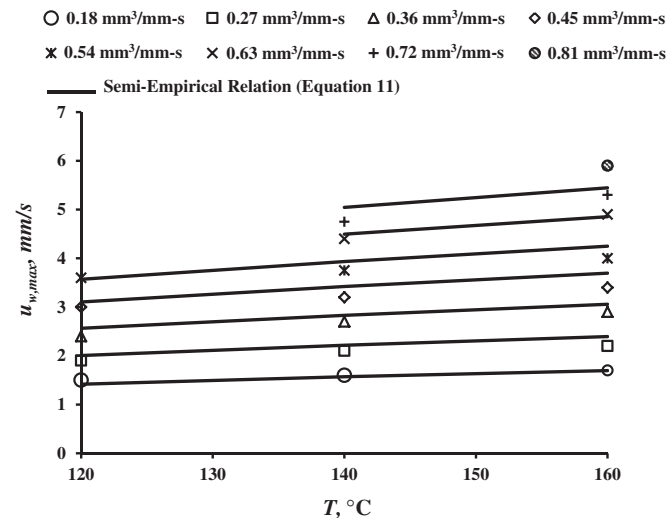
○ 0.30 mm³/mm-s   □ 0.60 mm³/mm-s   △ 0.90 mm³/mm-s   ◇ 1.20 mm³/mm-s
✳ 1.50 mm³/mm-s   ✕ 1.80 mm³/mm-s   + 2.10 mm³/mm-s   ◎ 2.40 mm³/mm-s
—— Semi-Empirical Relation (Equation 11)

Fig. 14. Effect of power-law index, n, on the maximum coating speed, $u_{w,max}$ for various flow rates per unit width, Q' at $W = 0.30$ mm, $H = 0.30$ mm and $T = 140\ °C$. The discrete data points represent the simulation results, while the solid lines are obtained from Equation (11).

5.4.3. Effect of temperature (consistency index)

The temperature of the coating solution has an indirect impact on the maximum coating speed due to the variation in properties (that appear in Equation (11)) of the coating solution with temperature; consistency index (k), power-law index (n) and surface tension (σ). The effect of temperature on the maximum coating speed is illustrated in Fig. 13 for various flow rates per unit width ranging from 0.18 mm³ mm⁻¹ s⁻¹ to 0.81 mm³ mm⁻¹ s⁻¹ at $W = 0.178$ mm and $H = 0.25$ mm s⁻¹. Since the viscosity lowers as the solution is heated to a higher temperature, an increase in the maximum coating speed is noticed when the solutions are processed at higher temperatures. Several researchers [60–62] have earlier demonstrated the inverse relationship between viscosity and temperature. Even though, there are advantages in processing the solution at higher temperatures in terms of achieving higher maximum coating speeds, there is a disadvantage in terms of using extra energy to heat the solution. The variation in surface tension and power-law index with temperature is within 5%, while the

○ 0.18 mm³/mm-s   □ 0.27 mm³/mm-s   △ 0.36 mm³/mm-s   ◇ 0.45 mm³/mm-s
✳ 0.54 mm³/mm-s   ✕ 0.63 mm³/mm-s   + 0.72 mm³/mm-s   ◎ 0.81 mm³/mm-s
—— Semi-Empirical Relation (Equation 11)

Fig. 13. Effect of processing temperature, T, on the maximum coating speed, $u_{w,max}$ for various flow rates per unit width, Q' at $W = 0.178$ mm and $H = 0.25$ mm. The discrete data points represent the simulation results, while the solid lines are obtained from Equation (11).
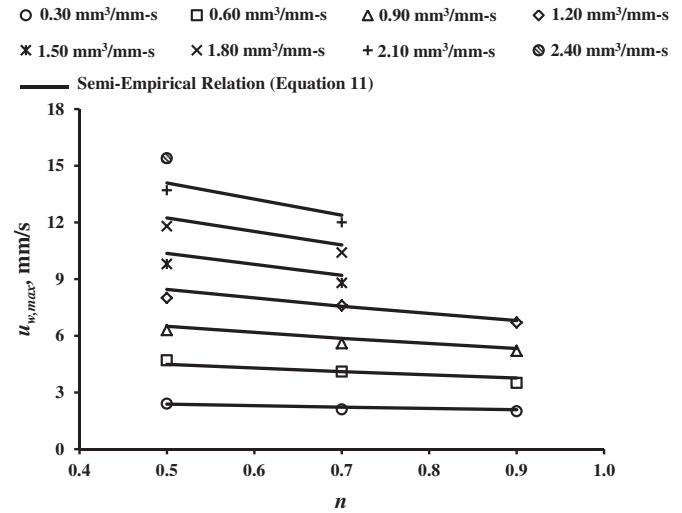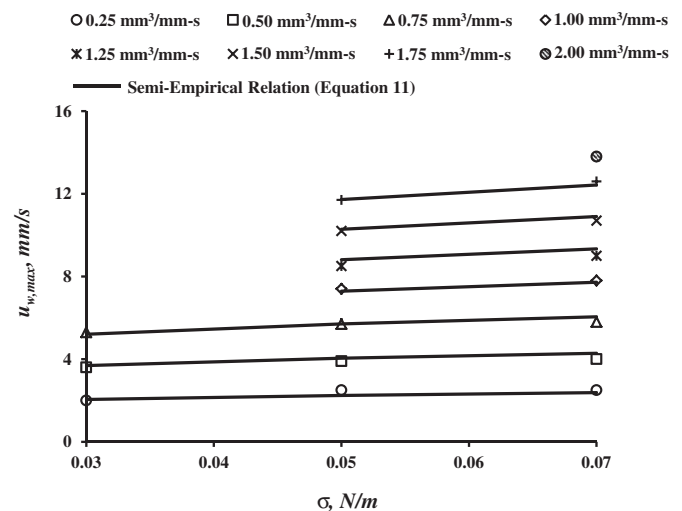
○ 0.25 mm³/mm-s   □ 0.50 mm³/mm-s   △ 0.75 mm³/mm-s   ◇ 1.00 mm³/mm-s
✳ 1.25 mm³/mm-s   ✕ 1.50 mm³/mm-s   + 1.75 mm³/mm-s   ◎ 2.00 mm³/mm-s
—— Semi-Empirical Relation (Equation 11)

Fig. 15. Effect of surface tension, σ, on the maximum coating speed, $u_{w,max}$ for various flow rates per unit width, Q' at $W = 0.25$ mm, $H = 0.25$ mm and $T = 160\ °C$. The discrete data points represent the simulation results, while the solid lines are obtained from Equation (11).

variation in consistency index is around 50%. Therefore, the impact of temperature on the maximum coating speed can be considered as an inverse impact of the consistency index on the maximum coating speed. The consistency index decreases as the temperature increases.

5.4.4. Effect of power-law index

The effect of power-law index (n ranging from 0.5 to 0.9) on maximum coating speed for Q' ranging from 0.30 mm^3 mm^{-1} s^{-1} to 2.40 mm^3 mm^{-1} s^{-1} at $W = 0.30$ mm, $H = 0.30$ mm, and $T = 140\,°C$, is depicted in Fig. 14. Due to the variation of viscosity as a function of $u_{w,max}^n$, there exists a larger impact of the power-law index at higher coating speeds, which are associated with higher flow rates per unit width. Another observation that can be made from the plot is that solutions that have low power-law index values can allow for lower viscosities, thereby increasing the coating speeds.

5.4.5. Effect of surface tension

The effect of surface tension on the maximum coating speed is illustrated in Fig. 15 at $W = 0.25$ mm, $H = 0.25$ mm, $T = 160\,°C$ and Q' ranging from 0.25 mm^3 mm^{-1} s^{-1} to 2.00 mm^3 mm^{-1} s^{-1}. In accordance with the findings discussed earlier in Section 5.2, solutions with lower surface tension and hence lower capillary number are subjected to coating bead instability, thereby restricting the maximum coating speed to lower values. Better stability experienced by higher surface tension solutions resulted in higher maximum coating speed, while allowing higher flow rates. These observations are consistent with the observations made by Chu et al. [14,26], Tiu et al. [25] and Burley and Kennedy [61].

Considering the results from this study, the maximum coating speeds were found to be independent of the slot gap and relatively insensitive to changes in surface tension and power-law index. The viscosity of a shear-thinning fluid can be changed through changing consistency or power-law indices. It has been shown that changing the power-law index, which indicates the degree of the shear-thinning behavior of the coating solution, has an insignificant impact on the maximum coating speed at higher flow rates. However, the maximum coating speeds were found to be sensitive to the consistency index and coating gap. Specifically, the coating gap sensitivity was dominate, a 40% increase in coating gap resulted in a 50% decrease in coating speed, while only a 10% change in coating speed was observed when the consistency index was increased by 50%. It should be mentioned that the conclusions made here are restricted to the ranges that were investigated in the current study.

6. Conclusions

The coating windows for shear-thinning, power-law fluids, which have apparent viscosities ranging from 1 Pa s to 20 Pa s, based on slot die coating were accurately predicted using numerical simulations. A two-dimensional VOF model available in FLUENT 6.3.26 was used to perform the simulations, which were validated experimentally using a RFIS. The effect of slot gap, coating gap and temperature on the coating window were studied by performing a fractional–factorial DOE. Based on the coating windows obtained from the DOE study, non-dimensionalized coating windows of the dimensionless minimum wet thickness with respect to capillary number were generated. The end of coating window was obtained when either the maximum capillary number approached 1.2 or the dimensionless minimum wet thickness ranged between 0.55 and 0.6. A semi-empirical model was derived from the non-dimensionalized coating windows that can predict the maximum coating speeds during slot die coating process. The maximum coating speeds were found to be independent of the slot gap values,

while smaller coating gaps facilitated higher maximum coating speeds. However, larger coating gaps provided versatility in the range of thicknesses that could be obtained for a given set of operational and processing conditions. Processing the coating solutions at higher temperatures resulted in a drop in the viscosity of the solutions, which led to an increase in the maximum coating speeds. Higher surface tension fluids facilitated stable coating beads, thus delaying air engulfment. Therefore, solutions with higher surface tension and hence higher capillary numbers can be processed at higher coating speeds.

Nomenclature

Roman alphabets

Ca	capillary number
F	force, N
f	function of any variable
g	gravity, m s^{-2}
h	wet thickness, mm
H	coating gap or stand-off height, mm
k	consistency index, Pa s^n
L	coating bead length, mm
m	number of parameters
n	power-law index
P	pressure, Pa
Q	flow rate, mm^3 s^{-1}
Q'	flow rate per unit slot die width, mm^3 mm^{-1} s^{-1}
Re	Reynolds number
r	distance from the contact line, mm
T	temperature, °C
t	time, s
u	x-velocity, mm s^{-1}
v	y-velocity, mm s^{-1}
W	slot gap, mm
x	space variable in the horizontal direction
y	space variable in the vertical direction

Greek symbols

α	volume fraction
η	apparent viscosity, Pa s
$\dot{\gamma}$	shear rate, s^{-1}
κ	curvature of the interface surface, mm^{-1}
μ	dynamic viscosity, Pa s
ϕ	angle made by the sawtooth structures with horizontal, °
ρ	density, kg m^{-3}
σ	surface tension, N m^{-1}
τ	shear stress tensor, Pa
θ	contact angle, °

Other symbols

$\mathscr{L}$	length, mm
ℓ	characteristic length, mm
n	index for time step
$\hat{\boldsymbol{n}}$	unit normal vector
φ	fluid property, kg m^{-3} for density, or Pa s for viscosity
$\mathfrak{T}$	stress tensor, Pa

$\mathscr{T}$	normal stress tensor, Pa
$\hat{\boldsymbol{t}}$	Unit tangent vector
$\mathscr{U}$	volume flux based on normal velocity, mm^3 s^{-1}
$\boldsymbol{u}$	velocity vector, mm s^{-1}
$\mathscr{V}$	volume, mm^3
$\bar{\sigma}$	characteristic velocity, mm s^{-1}
W	width, mm

Subscripts

a	apparent
air	air
c	contact line
cs	coating/coating solution
d	dynamic
dj	disjoining
f	film
f	face of a computational cell
g	gauge
i	index
if	interface
in	inlet
j	index
l	die lip
max	maximum
min	minimum
nd	non-dimensional
nl	normal
PET	PET (substrate)
s	static
st	sawteeth
sd	slot die
s	source
t	tangent
w	wall

References

[1] A.E. Beguin, U. S. Patent 2,681,694, 1954.
[2] T.M. Milbourn, J.J. Barth, U.S. Patent 5,360,629, 1994.
[3] E.J. Choinski, U.S. Patent 4,938,994, 1990.
[4] T.A.L. Harris, D.F. Walczyk, Journal of Manufacturing Processes 8 (2006) 8–20.
[5] T. Steenberg, H.A. Hjuler, C. Terkelsen, M.T.R. Sanchez, L.N. Cleemann, F.C. Krebs, Energy & Environmental Science 5 (2012) 6076–6080.
[6] K.L. Bhamidipati, S. Didari, P. Bedell, T.A.L. Harris, Journal of Non-Newtonian Fluid Mechanics 166 (2011) 723–733.
[7] C.-P. Chin, H.-S. Wu, S.S. Wang, Industrial and Engineering Chemistry Research 49 (2010) 3802–3809.
[8] O.J. Romero, M.S. Carvalho, Chemical Engineering Science 63 (2008) 2161–2173.
[9] E.B. Gutoff, C.E. Kendrick, AIChE Journal 33 (1987) 141–145.
[10] C.-Y. Ning, C.-C. Tsai, T.-J. Liu, Chemical Engineering Science 51 (1996) 3289–3297.
[11] C.K. Yang, D.S.H. Wong, T.J. Liu, Polymer Engineering and Science 44 (2004) 1970–1976.
[12] T.D. Blake, K.J. Ruschak, Nature 282 (1979) 489–491.
[13] B.V. Deryagin, S.M. Levi, Film Coating Theory, Focal Press, London, 1959.
[14] W.-B. Chu, J.-W. Yang, Y.-C. Wang, T.-J. Liu, C. Tiu, J. Guo, Journal of Colloid and Interface Science 297 (2006) 215–225.
[15] Y.-R. Chang, H.-M. Chang, C.-F. Lin, T.-J. Liu, P.-Y. Wu, Journal of Colloid and Interface Science 308 (2007) 222–230.
[16] H. Benkreira, M.I. Khan, Chemical Engineering Science 63 (2008) 448–459.
[17] M.S. Carvalho, H.S. Kheshgi, AIChE Journal 46 (2000) 1907–1917.
[18] O.J. Romero, L.E. Scriven, M.S. Carvalho, Journal of Non-Newtonian Fluid Mechanics 138 (2006) 63–75.
[19] H.-M. Chang, Y.-R. Chang, C.-F. Lin, T.-J. Liu, Polymer Engineering and Science 47 (2007) 1927–1936.
[20] C.-F. Lin, D.S.H. Wong, T.-J. Liu, P.-Y. Wu, Advances in Polymer Technology 29 (2010) 31–44.
[21] K.-Y. Lee, L.-D. Liu, L. Ta-Jo, Chemical Engineering Science 47 (1992) 1703–1713.
[22] Y.-R. Chang, C.-F. Lin, T.-J. Liu, Polymer Engineering and Science 49 (2009) 1158–1167.
[23] O.J. Romero, W.J. Suszynski, L.E. Scriven, M.S. Carvalho, Journal of Non-Newtonian Fluid Mechanics 118 (2004) 137–156.
[24] C. Hamers, M. Schatl, E. Krumbacher, O. Birkert, U. Fröhlich, M. Tietz, N. Gerteiser, Pulp and Paper International 47 (2005) 36–37.
[25] C. Tiu, L. Wang, T.-J. Liu, Journal of Non-Newtonian Fluid Mechanics 87 (1999) 247–261.
[26] W.-B. Chu, J.-W. Yang, T.-J. Liu, C. Tiu, J. Guo, Colloids and Surfaces A: Physicochemical and Engineering Aspects 302 (2007) 1–10.
[27] K.J. Ruschak, Chemical Engineering Science 31 (1976) 1057–1060.
[28] B.G. Higgins, L.E. Scriven, Chemical Engineering Science 35 (1980) 673–682.
[29] H. Saito, L.E. Scriven, Journal of Computational Physics 42 (1981) 53–76.
[30] O.J. Romero, L.E. Scriven, M.S. Carvalho, AIChE Journal 52 (2006) 447–455.
[31] C.W. Hirt, B.D. Nichols, Journal of Computational Physics 39 (1981) 201–225.
[32] C.W. Hirt, J.E. Richardson, Simulation of Transient and Three-dimensional Coating Flows Using a Volume-of-fluid Technique, in: 50th Annual Conference of the Society for Imaging and Science Technology, Boston (1997).
[33] T.A.L. Harris, K.L. Bhamidipati, ECS Transactions 12 (2008) 251–262.
[34] K.L. Bhamidipati, T.A.L. Harris, ASME Conference Proceedings 2009 (2009) 695–702.
[35] K.L. Bhamidipati, T.A.L. Harris, Journal of Fuel Cell Science and Technology 7 (2010) 061005.
[36] K.L. Bhamidipati, T.A.L. Harris, Polymer Engineering and Science (2010).
[37] K.L. Bhamidipati, Detection and Elimination of Defects During Manufacture of High-temperature Polymer Electrolyte Membranes, George Woodruff School of Mechanical Engineering, Georgia Institute of Technology, Atlanta, 2011.
[38] T.A.L. Harris, Design Methodology, Science, and Technology to Manufacture High Temperature Polymer Electrolyte Membranes for Fuel Cells, Mechanical Engineering, Rensselaer Polytechnic Institute, Troy, 2006.
[39] J. Johnson, T. Harris, Applied Optics 49 (2010) 2920–2928.
[40] FLUENT, User Guide Fluent 6.3. (2006). Lebanon, NH.
[41] D.L. Young, Numerical Methods for Fluid Dynamics (1982) 273–285.
[42] J.U. Brackbill, D.B. Kothe, C. Zemach, Journal of Computational Physics 100 (1992) 335–354.
[43] C. Huh, L.E. Scriven, Journal of Colloid and Interface Science 35 (1971) 85–101.
[44] D.H. Michael, Mathematika 5 (1958) 82–84.
[45] H.K. Moffatt, Journal of Fluid Mechanics 18 (1964) 1–18.
[46] Y.D. Shikhmurzaev, Moving Contact Lines, in: Capillary Flows with Forming Interfaces, Chapman & Hall, 2007.
[47] S.F. Kistler, The Fluid Mechanics of Curtain Coating and Related Viscous Free Surface Flows with Contact Lines, University of Minnesota, 1983.
[48] E.B. Dussan V, S.H. Davis, Journal of Fluid Mechanics 65 (1974) 71–95.
[49] F. Brochard, P.G. De Gennes, Langmuir 8 (1992) 3033–3037.
[50] E.B. Dussan V, Annual Review of Fluid Mechanics 11 (1979) 371–400.
[51] E.B. Dussan V, Journal of Fluid Mechanics 77 (1976) 665–684.
[52] F.Y. Kafka, E.B. Dussan, Journal of Fluid Mechanics 95 (1979) 539–565.
[53] M. Renardy, Y. Renardy, J. Li, Journal of Computational Physics 171 (2001) 243–263.
[54] S. Rosenblat, S.H. Davis, How Do Liquid Drops Spread on Solids? Springer-Verlag, Berlin, West Ger, 1985, pp. 171–183.
[55] W.J. Silliman, Viscous Film Flows with Contact Lines: Finite Element Simulation, a Basis for Stability Assessment and Design Optimization, University of Minnesota, 1979.
[56] P.A. Thompson, M.O. Robbins, Physical Review Letters 63 (1989) 766.
[57] D.E. Weidner, L.W. Schwartz, Physics of Fluids 6 (1994) 3535–3538.
[58] R.T. Scharenberg, Encyclopedia of Polymer Science and Technology, Wiley-Interscience, New York, 1985.
[59] W.L. Wilkinson, Chemical Engineering Science 30 (1975) 1227–1230.
[60] R. Burley, R.P.S. Jolly, Chemical Engineering Science 39 (1984) 1357–1372.
[61] R. Burley, B.S. Kennedy, Chemical Engineering Science 31 (1976) 901–911.
[62] E.B. Gutoff, C.E. Kendrick, AIChE Journal 28 (1982) 459–466.